ACS APPLIED MATERIALS & INTERFACES

Research Article

www.acsami.org

Nitrogen-Doped Carbon Nanocoil Array Integrated on Carbon Nanofiber Paper for Supercapacitor Electrodes

Won Ho Choi,[†] Mi Jin Choi,[†] and Jin Ho Bang*[,†,‡]

[†]Department of Bionanotechnology and [‡]Department of Chemistry and Applied Chemistry, Hanyang University, 55 Hanyangdaehak-ro, Sangnok-gu, Ansan, Kyeonggi-do 15588, Republic of Korea

Supporting Information

ABSTRACT: Integrating a nanostructured carbon array on a conductive substrate remains a challenging task that presently relies primarily on high-vacuum deposition technology. To overcome the problems associated with current vacuum techniques, we demonstrate the formation of an N-doped carbon array by pyrolysis of a polymer array that was electrochemically grown on carbon fiber paper. The resulting carbon array was investigated for use as a supercapacitor electrode. In-depth surface characterization results revealed that the microtextural properties, surface functionalities, and degree of nitrogen incorporated into the N-doped carbon array can be delicately controlled by manipulating carbonization temperatures. Furthermore, electrochemical measurements showed that subtle changes in these physical properties resulted in significant changes in the capacitive behavior of the N-doped carbon array. Pore structures and nitrogen/oxygen functional groups, which are favorable for charge storage, were formed at low carbonization temperatures. This result showed the importance of having a comprehensive understanding of how the surface characteristics of carbon affect its capacitive performance. When utilized as a substrate in a pseudocapacitive electrode material, the N-doped carbon array maximizes capacitive performance by simultaneously achieving high gravimetric and areal capacitances due to its large surface area and high electrical conductivity.

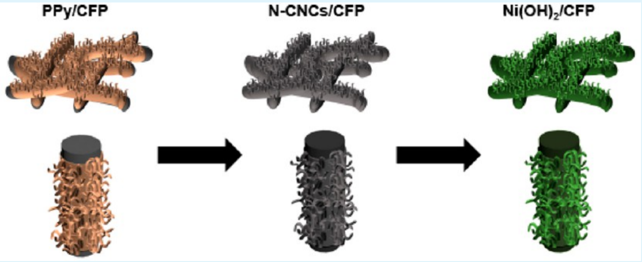

KEYWORDS: *carbon array, N-doping, surface functionality, pore size, capacitance*

1. INTRODUCTION

Carbon has a unique role as an important electrode component in various energy conversion and storage applications.[1−3] For instance, graphite has long been employed as an anode material in Li-ion batteries (LIBs) and activated carbons (e.g., MSP-20 from Kansai and YP-50F from Kuraray) are used as a host material for charge storage in electrochemical double-layer capacitors (EDLCs). Carbon blacks such as Vulcan XC72R, Ketjenblack, and Super P, have served as excellent supports for fuel cell catalysts and as a conductive additives in LIB and pseudocapacitor electrodes. Furthermore, nanostructured carbon allotropes (e.g., fullerenes, carbon nanotubes, and graphene) have found uses in solar cells and LIBs.

Carbon products primarily come in the form of a powder. Despite the advantages of dealing with carbon powders, their use is hampered by practical constraints. Powder-form carbon must be mixed with polymeric binders so they can be applied onto a conductive substrate. The use of binders hinders the diffusion of electrolyte resulting in severe agglomeration of carbon particles and poor connections between them. The full benefits of the surface area and electrical conductivity of carbon are not realized because of these problems. These limitations are more critical when carbon powders are utilized as a main active electrode material, as in EDLCs. Given the charge storage mechanism involved in EDLCs (i.e., reversible ion adsorption on the carbon surface only), it is highly desirable to design a binder-free, large-surface-area carbon electrode having well-defined porous structures. Several strategies have been developed to fabricate binder-free carbon electrodes, including graphene monoliths, carbon nanotube/graphene films (or fibers), and carbon nanotube arrays.[4−10] The benefits of these binder-free carbon arrays were maximized when large-surface-area, nanostructured carbon was integrated into an array on a conductive substrate. This strategy offers excellent electrical connection to the conductive substrate, enables fast electron transport, and facilitates electrolyte diffusion. A recent article on rationally designed carbon nanotube forests is a good example that demonstrates the improvements obtained using integrated carbon.[11] Goodenough and co-workers also reported an electrode based on carbon nanotubes assembled on carbon nanofibers; their work highlighted the benefits of carbon arrays in charge storage devices.[12]

Integrating carbon nanostructures on a conductive substrate remains quite challenging, partly because it relies primarily on a high-vacuum technology such as chemical vapor deposition (CVD).[11−16] While CVD processes for the growth of carbon

Received: June 22, 2015
Accepted: August 12, 2015
Published: August 12, 2015

DOI: 10.1021/acsami.5b05527
ACS Appl. Mater. Interfaces 2015, 7, 19370−19381

Scheme 1. Schematic Illustration of the Synthesis of a N-CNC Array

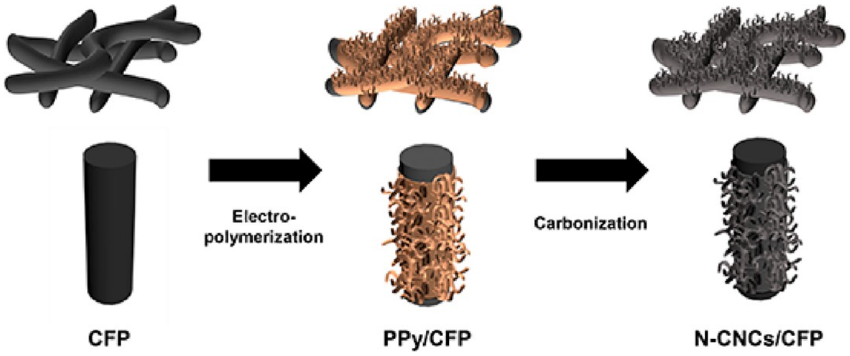

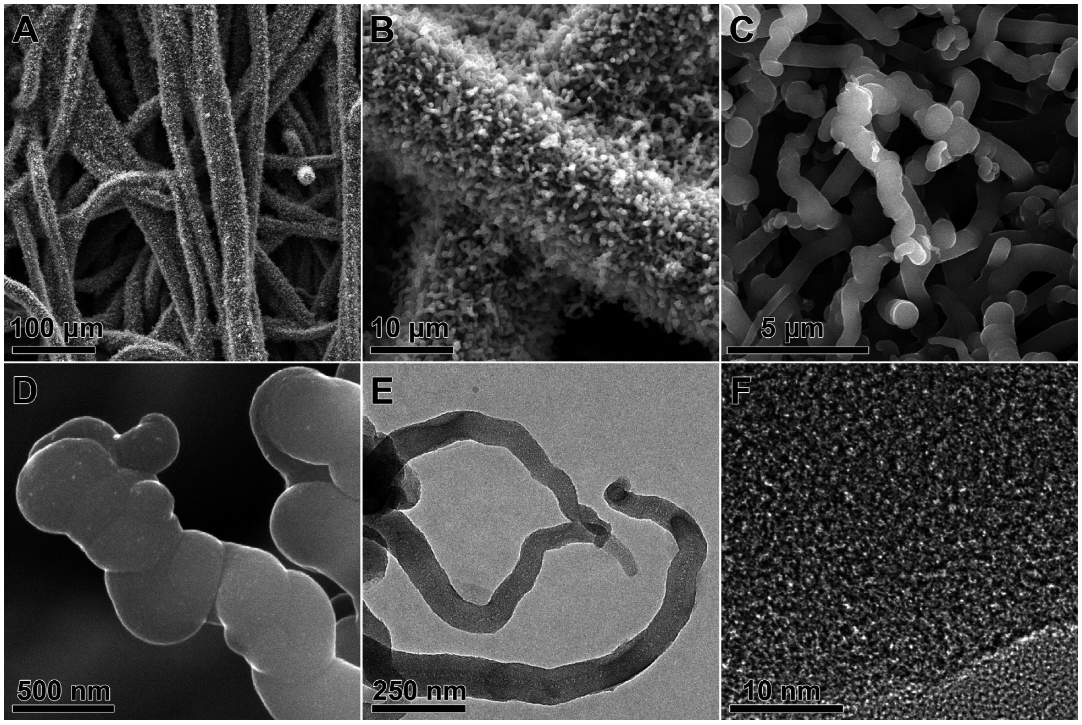

Figure 1. (A–D) SEM and (E,F) TEM images of N-CNCs obtained after carbonization at 700 °C.

nanoarrays are well-developed, CVD requires expensive equipment and high temperatures; furthermore, the use of CVD is often inadequate when the substrate for carbon growth is electrically conductive.[17] Therefore, a low-cost, generalizable approach for the deposition of carbon nanoarrays on a conductive substrate is of great interest.

In the present work, we demonstrate that the electropolymerization of pyrrole followed by the carbonization of polypyrrole (PPy) is a facile, reproducible synthetic route to obtain N-doped carbon arrays integrated onto conductive substrates. Not only does this novel approach require no high-cost equipment, but it also allows for delicate control over the microtextural properties and surface functionality of carbon (i.e., nitrogen- and oxygen-containing surface groups) by changing the carbonization temperature. Our in-depth surface analysis revealed that controlling these surface characteristics (i.e., pore size and the nature of the heteroatoms) is critical to boosting the capacitance and rate performance of the N-doped carbon arrays. Further, we demonstrate that this newly designed carbon array could be employed as a large-surface-area, conductive substrate for various pseudocapacitive materials. A $Ni(OH)_2$ electrode was prepared as a model system using this carbon array and was evaluated for use as a pseudocapacitor electrode. Both gravimetric and areal capacitances of the $Ni(OH)_2$ electrode were found to be superior to those of other $Ni(OH)_2$ electrodes in the literature. This excellent performance was attributed to the benefits from the N-doped carbon array including (i) a large surface area that enables a high loading of electroactive materials in the form of a thin, uniform film, (ii) a high electrical conductivity that allows for fast electron transport, and (iii) a porous structure that offers easy access of electrolyte to the surface of electroactive materials.

2. EXPERIMENTAL SECTION

2.1. Preparation of Nitrogen-Doped Carbon Nanocoil (N-CNC) Arrays. N-CNC arrays were prepared by the carbonization of a PPy array deposited on a piece of carbon fiber paper (CFP, SGL Technology) via the electropolymerization of pyrrole. Pyrrole monomer (150 mM), Na_2HPO_4 (200 mM), and $LiClO_4$ (2 mM) were dissolved in deionized water (100 mL).[18] The solution was then warmed at 25 °C using a water bath and was used as the electrolyte. The electrochemical polymerization of pyrrole was conducted under a three-electrode system wherein the CFP piece was the working electrode, an Ag/AgCl electrode

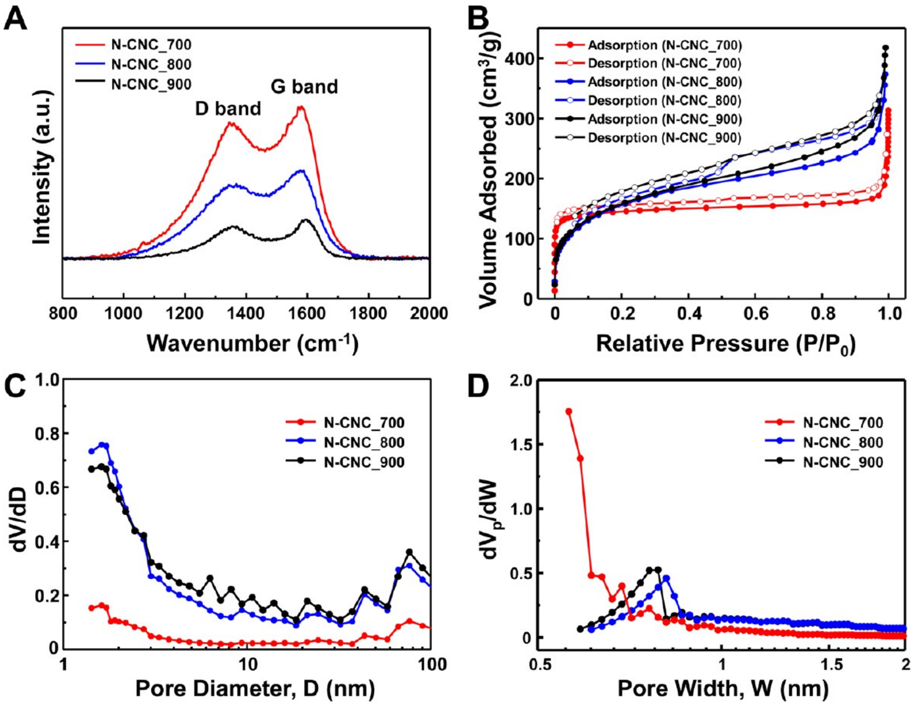

Figure 2. (A) Raman spectra, (B) N_2 adsorption/desorption isotherm, (C) pore size distribution obtained using the BJH model, and (D) pore size distribution of micropore regions obtained using the T-plot method of N-CNCs obtained at different temperatures.

Table 1. Structural Parameters of N-CNCs Obtained from Nitrogen Adsorption Isotherm

	S_{BET} (m^2/g)	V_{total} (cm^3/g)	S_{micro} (m^2/g)	V_{micro} (cm^3/g)	S_{meso} (m^2/g)	V_{meso} (cm^3/g)	mean pore diameter (nm)
N-CNC_700	567.0	0.308	543.2	0.221	23.8	0.087	2.2
N-CNC_800	582.4	0.575	441.8	0.212	140.6	0.363	3.9
N-CNC_900	583.4	0.639	384.3	0.184	199.1	0.455	4.4

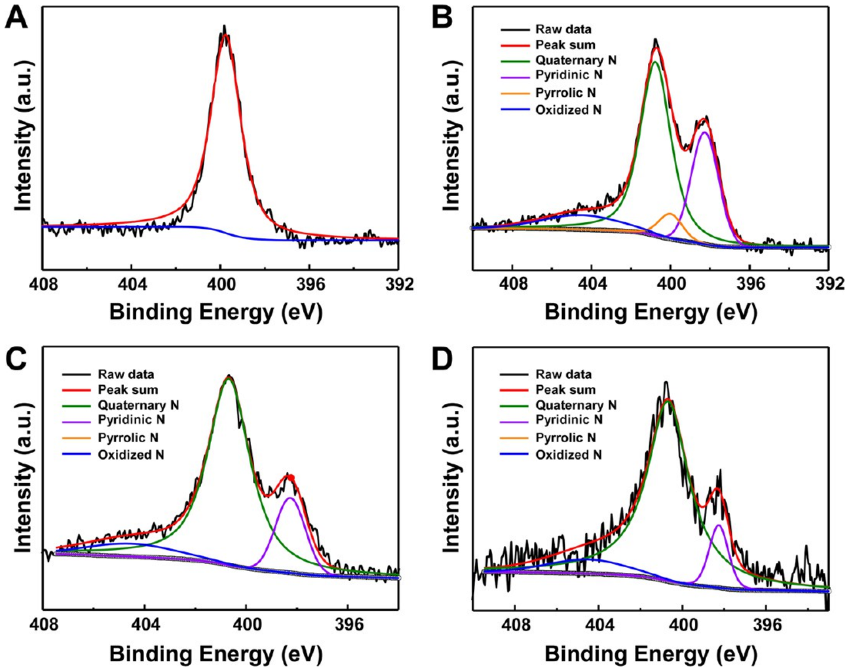

Figure 3. XPS N 1s spectra of (A) PPy and N-CNCs obtained at (B) 700 °C, (C) 800 °C, and (D) 900 °C.

was the reference electrode, and a platinum foil was the counter electrode. A potential of 0.9 V (vs Ag/AgCl) was applied for 3 h to effect the polymerization of pyrrole. The resulting PPy array deposited on CFP was rinsed with deionized water, dried in air, and was subsequently annealed under a N_2 atmosphere at different temperatures (700, 800, and 900 °C) to convert the PPy array into a N-CNC array. The N-CNC

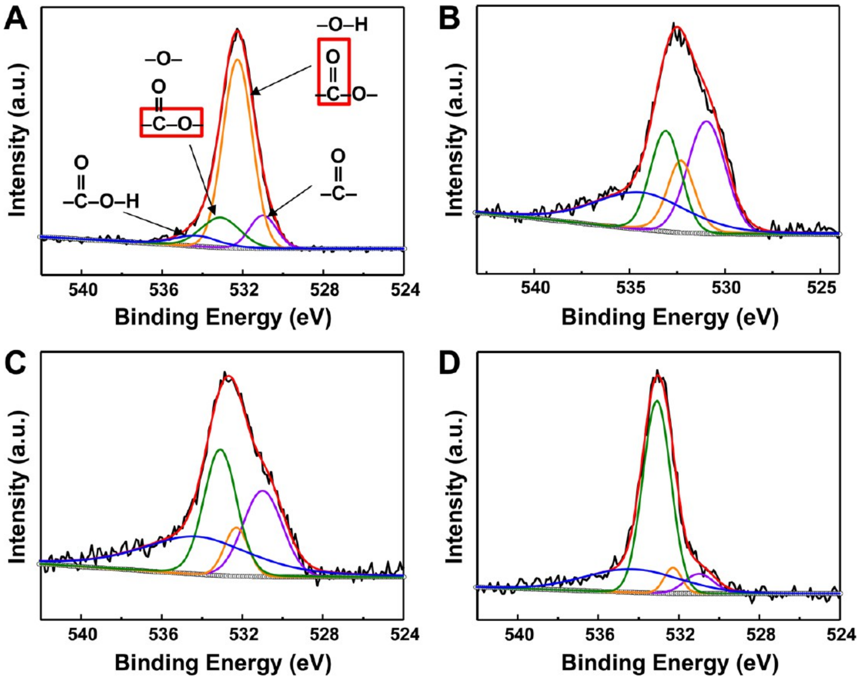

Figure 4. XPS O 1s spectra of (A) PPy and N-CNCs obtained at (B) 700 °C, (C) 800 °C, and (D) 900 °C.

arrays prepared at 700, 800, and 900 °C will hereafter be referred to as N-CNC_700, N-CNC_800, and N-CNC_900, respectively. To demonstrate the versatility of our approach to other substrates, we performed the electropolymerization on Pt film deposited on a quartz plate using a Pt sputter equipment. The electrochemical deposition was carried out using the above-mentioned three-electrode system with a potential of 3 V applied for 10 min.

2.2. Electrodeposition of $Ni(OH)_2$ on N-CNC and CFP. A thin layer of $Ni(OH)_2$ was deposited over the N-CNC_700 (or CFP) substrate using an electrochemical deposition method as previously reported.[19] The electrochemical deposition was performed under the same three-electrode system employed for the PPy deposition in a 0.1 M $Ni(NO_3)_2$ solution heated to 65 °C. Potentials of 0.55 V (for the N-CNC substrate) and 0.66 V (for the CFP substrate) vs Ag/AgCl were applied for 180 s each. Because the surface area of the CFP was much smaller than that of the N-CNC, a more negative potential was required for the CFP substrate to ensure that sufficient columbic charge was available for the deposition. The quantity of $Ni(OH)_2$ deposited on each substrate was weighed using a microbalance (A&D BM-22, readability to 1 μg), and the loading was determined to be 4.8 mg for both electrodes (area: 2.5 cm^2).

2.3. Characterization and Electrochemical Measurements. Characterization of the N-CNC array and $Ni(OH)_2$/N-CNC was carried out using scanning electron microscopy (SEM, Hitachi S-4800), transmission electron microscopy (TEM, JEOL-2100F), X-ray photoelectron spectroscopy (XPS, PHI Versa Probe system), and Raman spectroscopy (Renishaw RM-1000). Fourier transform-infrared (FT-IR) spectra were recorded using a Varian FTS 1000 spectrophotometer. N_2 adsorption/desorption isotherms were obtained for the N-CNC arrays at 77 K using a surface area analyzer (Bel Japan Belsorp Mini II). The adsorption branches were used to calculate the total pore volume (V_{total}), the specific surface area (S_{BET}), and the pore size distribution. S_{BET} values were obtained using the Brunauer–Emmett–Teller (BET) method, and the pore size distributions were analyzed using the Barrett–Joyner–Halenda (BJH) model. The specific surface area (S_{micro}) and the total pore volume (V_{micro}) originating only from the micropores were calculated using the T-plot method. All electrochemical measurements were performed using a CHI 660D electrochemical workstation at room temperature. The capacitive performance of N-CNCs, $Ni(OH)_2$/N-CNC, and $Ni(OH)_2$/CFP electrodes prepared without any binders and conductive agents was investigated using a three-electrode configuration with Hg/HgO as the reference electrode and a platinum wire as the counter electrode in 1 M KOH electrolyte. Electrochemical impendence spectroscopy (EIS) was conducted in the frequency range of 0.01 Hz to 100 kHz with a perturbation amplitude of 5 mV. To fabricate a symmetric capacitor (N-CNC//N-CNC), two pieces of N-CNC_700 and a filter paper soaked in 1.0 M KOH were used as electrodes and a separator, respectively. When assembled together, the symmetric capacitor was evaluated using cyclic voltammetry (CV) and galvanostatic charge–discharge test.

3. RESULTS AND DISCUSSION

Carbon arrays were fabricated on various substrates via CVD in several previous reports.[11,13,14,16] This method typically involves the deposition of a transition metal catalyst, such as Fe and Ni, followed by the controlled pyrolysis of carbon precursors (e.g., methane, ethylene, or pyridine) at elevated temperatures. Here, we introduce a simple wet-chemical process based on the electropolymerization of pyrrole and subsequent carbonization of the resulting polymer array as a facile alternative route to prepare carbon arrays on a conductive substrate. Scheme 1 depicts the overall procedure of the preparation of N-CNC arrays. Electrochemical polymerization of pyrrole has been well-studied because of its intriguing physical properties. In a typical procedure, the polymerization was initiated by the formation of radical cations created by electrochemical oxidation and it proceeds through the continual coupling of these radical species.[20] In our work, pyrrole was deposited on CFP in a one-dimensional array without the use of a template by delicately suppressing overoxidation of PPy.[21] CFP was chosen as a freestanding, conductive substrate because of its various benefits that have been demonstrated in recent reports.[22−27] Figure S1 in the Supporting Information (SI) shows SEM images of a PPy array on CFP after electropolymerization. A uniform, compact polymer array was clearly observed on which PPy nanowires (hundreds of nanometers in diameter and tens of microns in length) were twisted into coil-shaped chains. The fabrication of PPy array is also applicable to other substrates. As a simple demonstration, Pt film sputtered on a quartz plate was used for

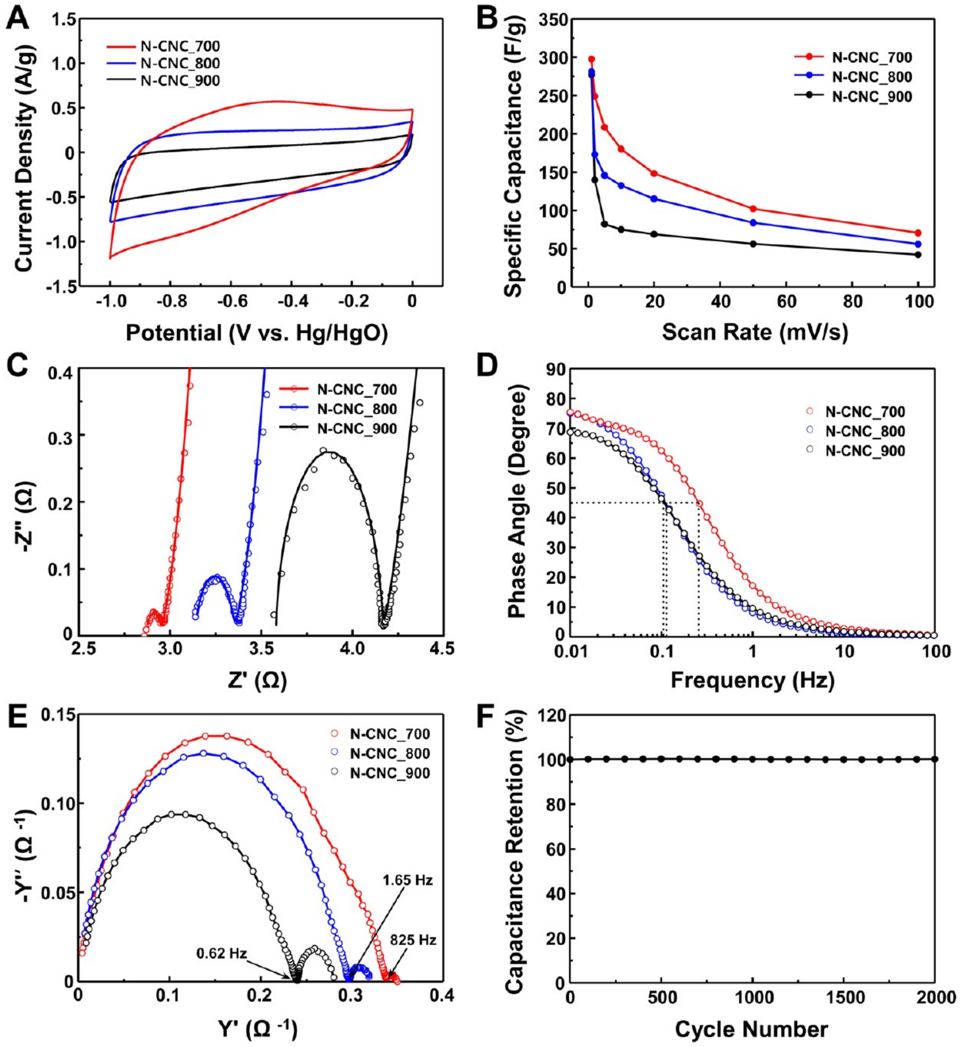

Figure 5. (A) Cyclic voltammograms (at 5 mV/s), (B) specific capacitances, (C) Nyquist plots (raw data with fitting lines), (D) frequency-dependent phase angle plots, and (E) admittance plots of N-CNCs obtained at different temperatures. (F) Long-term cycling performance of N-CNC_700.

Table 2. Relative Surface Contents of Nitrogen and Oxygen Species of N-CNCs

	N-5	N-6	N-Q	N-O	N content (atomic %)	N-6/N-Q ratio	O-I	O-II	O-III	O-IV
N-CNC_700	5.5	26.3	58.5	9.6	8.5	0.51	31.3	16.5	23.2	29.0
N-CNC_800		15.8	76.0	8.3	6.1	0.17	24.2	8.3	31.1	36.3
N-CNC_900		9.5	82.2	8.4	3.1	0.09	6.5	5.2	62.5	25.7

Table 3. EIS Parameters Extracted from Nyquist Plots of N-CNCs Obtained at Different Temperatures[a]

	R_1 (Ω)	R_2 (mΩ)	Q_1 (μF/s ^{a_1})	a_1	A_w (Ω/s ^{05})
N-CNC_700	2.87	75	992	0.89	0.48
N-CNC_800	3.14	208	257	0.88	0.54
N-CNC_900	3.58	580	22	0.96	0.55

[a] Impedance from CPE (Z_{CPE}), $Z_{CPE}(f) = 1/(Q_n(j2\pi f)^{a_n})$, where Q_n is the CPE parameter and a_n is the CPE exponent. Warburg impedance $(W) = A_w/(j\omega)^{0.5}$, where A_w is the Warburg coefficient, j is the imaginary unit, and ω is the angular frequency.

an electrode onto which PPy nanowires grew. A similar PPy array was observed under SEM analysis (Figure S2 in Supporting Information), highlighting the versatility of this electropolymerization approach.

Upon heat-treatment under an inert atmosphere, the PPy array was converted into a N-CNC array. Figure 1 displays the electron micrographs of the resulting N-CNC array obtained at 700 °C. N-CNC arrays synthesized at higher temperatures showed identical morphological features. It is evident from the SEM images (Figure 1A–D) that the original morphology of PPy remained largely intact after the carbonization demonstrating that the N-CNC array successfully retained the unique nanostructure of the PPy array. TEM images in Figure 1E,F revealed the amorphous, porous nature of the N-CNC array. These PPy arrays can serve as excellent precursors that yield heavily N-doped carbon due to their high N content (~16 wt %) and distinctive structural characteristics resulting from the template-less electropolymerization.[28−30] To avoid additional synthetic steps and to enable a high degree of nitrogen incorporation, direct carbonization of N-containing precursors

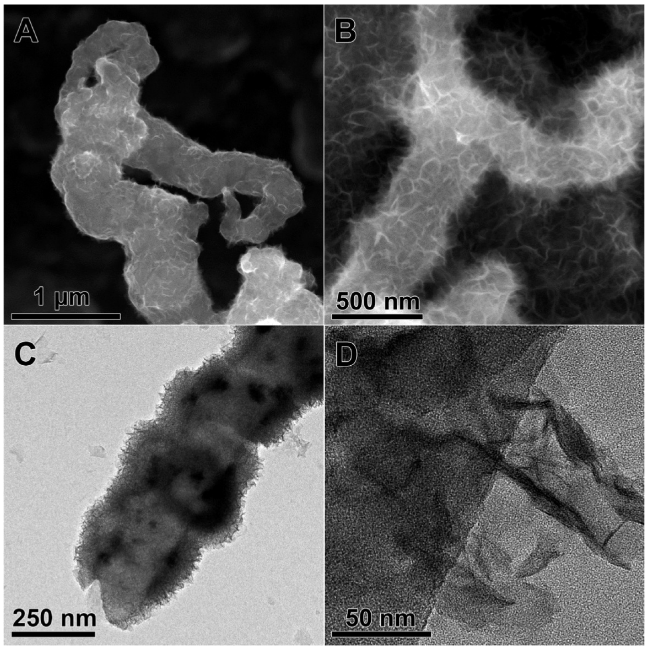

Figure 6. (A,B) SEM and (C,D) TEM images of $Ni(OH)_2$/N-CNCs.

has been preferred over a postheat treatment preformed under ammonia gas.

The degree of graphitization of N-CNC arrays was examined by Raman spectroscopy. Regardless of the carbonization temperature, the main Raman spectra features (i.e., the ratio of the intensities of D- and G-bands) were almost same for all the N-CNC arrays with a margin of error. Figure 2A shows two characteristic peaks at ~1350 and ~1580 cm^{-1} resulting from vibration modes (D- and G-band) of sp^3- and sp^2-hybridized carbon, respectively. The D band is associated with defects and disorder in the carbon network, whereas the G band is associated with graphitic carbon.[31] Given the ratio of the peak intensities from these two bands (0.84−0.90), a low degree of graphitization occurred, which is in agreement with the TEM analysis.

The textural characteristics of N-CNC arrays were examined by N_2 adsorption/desorption isotherm measurements. Figure 2B displays the isotherms of N-CNC_700, N-CNC_800, and N-CNC_900. All the isotherms simultaneously exhibited type I/IV features implying the presence of both micro- and mesopores in the N-CNC array. Unlike N-CNC_800 and N-CNC_900, N-CNC_700 showed a steeper rise in the low relative pressure region accompanied by a small hysteresis loop. This indicates that N_2 uptake by micropores prevails over uptake by meso/macropores in N-CNC_700. More prominent hysteresis loops were observed in the N-CNC_800 and N-CNC_900 implying that these materials had fewer micropores than N-CNC_700.

The textural parameters of N-CNCs are summarized in Table 1. S_{BET} increased slightly with increasing carbonization temperature, but there was a noticeable increase in V_{total} and mean pore diameter; the latter is ascribed to pore widening due to accelerated carbon burnoff at elevated temperatures.[30] S_{micro} and V_{micro} dramatically increased as the carbonization temperature decreased. In particular, S_{micro} was as large as 543.2 m^2/g (close to S_{BET} of 567 m^2/g) in the case of N-CNC_700 indicating that a large portion of pores were micropores. The pore size distribution obtained using the BJH model (Figure 2C) reveals that the majority of pores are less than 4 nm, suggesting that micropores and small mesopores are primarily responsible for the surface area of the N-CNC array. Figure 2D shows the pore size distribution in the micropore region, which reveals that the majority of micropores in each N-CNC array are less than 1 nm. In contrast to N-CNC_800 and N-CNC_900, N-CNC_700 shows a broader distribution down to ~0.55 nm.

The presence of N atoms incorporated into the N-CNC array was confirmed by XPS analysis (Figure S3 in the Supporting

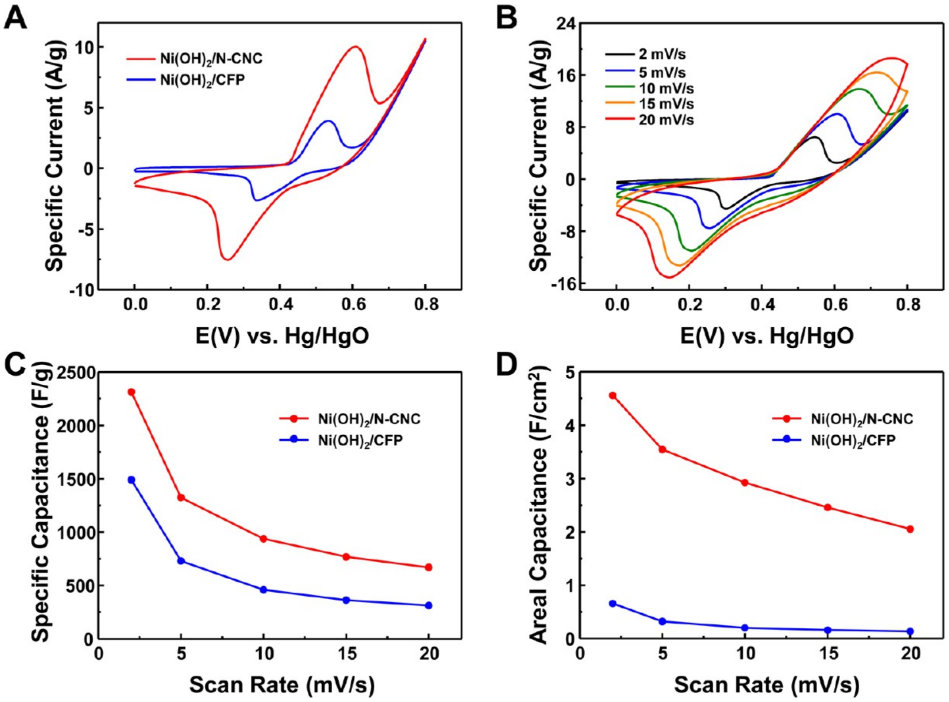

Figure 7. (A) Cyclic voltammograms of $Ni(OH)_2$/N-CNC and $Ni(OH)_2$/CFP at 5 mV/s, (B) cyclic voltammograms of $Ni(OH)_2$/N-CNC at various scan rates, (C) gravimetric capacitances, and (D) areal capacitances of $Ni(OH)_2$/N-CNC and $Ni(OH)_2$/CFP at different scan rates.

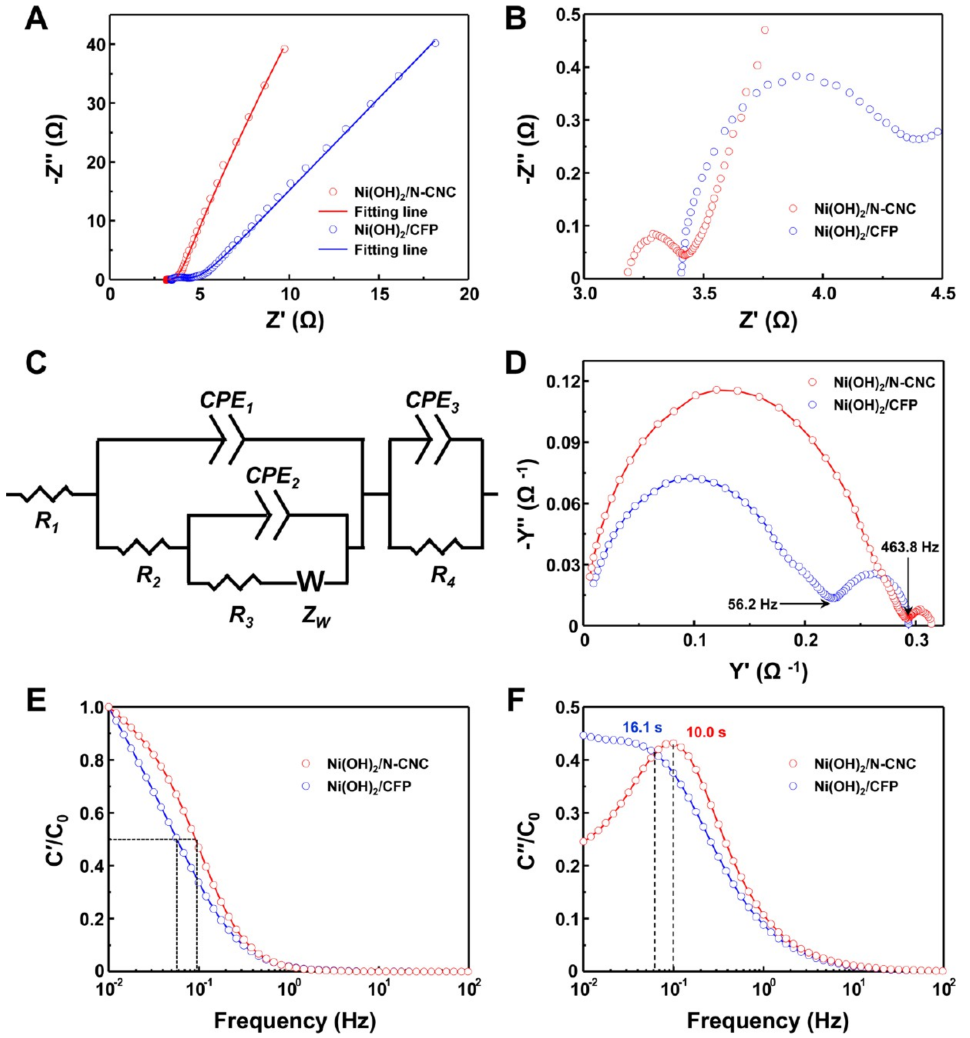

Figure 8. (A) Nyquist plots of $Ni(OH)_2$/N-CNC and $Ni(OH)_2$/CFP (raw data with fitting lines), (B) enlarged plots at high-frequency region, (C) equivalent circuit used to fit Nyquist plots (R_1, equivalent series resistance; R_2, charge transfer resistance representing deposition or desorption of an electroactive species; R_3, charge transfer resistance; R_4, leakage resistance; CPE_1, double layer capacitance; CPE_2, faradaic capacitance; CPE_3, pseudocapacitance; and Z_w, Warburg impedance), (D) admittance plots, (E) normalized real part of the capacitance as a function of frequency, and (F) normalized imaginary part of the capacitance as a function of frequency (C_0 is the full capacitance).

Table 4. EIS Parameters Extracted from Nyquist Plots of $Ni(OH)_2$/N-CNC and $Ni(OH)_2$/CFP

	R_1 (Ω)	R_2 (Ω)	R_3 (Ω)	Q_1 (F/s^{a_1})	a_1	Q_2 (F/s^{a_2})	a_2	A_w (Ω/$s^{0.5}$)
$Ni(OH)_2$/CFP	3.36	0.59	614.9	0.00043	0.99	0.22	0.82	296.70
$Ni(OH)_2$/N-CNC	3.19	0.18	3.37	0.00039	0.90	0.32	0.94	90.27

Information shows a survey scan and Figure 3 shows high resolution scans). Figure S3 shows that denitrogenation occurred, as is evident for the decrease in the intensity of the N peak with increasing temperature. Denitrogenation occurred more rapidly at elevated temperatures (Table 1), as is evident by the gradual decrease in the relative portion of C−N peaks in the XPS C 1s spectra with temperature (Figure S4 in the Supporting Information). The surface nitrogen content in N-CNC_700 was as high as 8.5 atomic wt %, whereas those in N-CNC_800 and N-CNC_900 were 6.1 and 3.1 atomic wt %, respectively. Figure 3A shows the XPS spectrum of PPy in the region of N 1s, where a single peak appears at 399.8 eV corresponding to N atoms in the PPy ring. During the carbonization process, chains of five-membered rings of PPy can be reorganized into a two-dimensional, hexagonal carbon lattice network (Scheme S1 in the Supporting Information). Depending on the position of N atoms in the carbon network, the substituted N species can be classified as pyridinic (N-6), pyrrolic (N-5), quaternary (N-Q), and oxidized N (N-O); these peaks appear at about 398.3, 399.9, 400.8, and 404.4 eV in the XPS spectra, respectively.[32] The XPS N 1s spectra of N-CNC_700, N-CNC_800, and N-CNC_900 are presented in Figure 3B−D. It is clear that the intensity of the N-5 rapidly decreased, while the peaks from N-6 and N-Q become much more pronounced after the heat-treatment. In addition, regardless of the carbonization temperature, N-6 and N-Q species prevail over N-5 and N-O species. This observation suggests that N atoms in the PPy ring tend to be incorporated primarily into the N-6 and N-Q positions in the carbon network. The ratios of N-6 to N-Q dramatically decreased as the carbonization temperature increased (Table 1); this was attributed to the better thermal stability of N-Q species over N-6 at elevated temperatures.[30] This trend in the N-6/N-Q ratios suggests that N atoms are more abundant at the edge of the graphene layer rather than in the inner graphene layer in the N-CNC_700 as compared to the other samples. Figure 4 displays the XPS O 1s spectra of PPy, N-CNC_700, N-CNC_800, and N-CNC_900. The XPS spectra can be deconvoluted into four different types of oxygen functionalities: carbonyl oxygen of quinones (O-I), carbonyl oxygen atoms in esters, anhydrides, and oxygen atoms in hydroxyl groups (O-II), noncarbonyl (ether-type) oxygen atoms in esters and anhydrides (O-III), and carboxylic groups with COOH or adsorbed water and/or oxygen (O-IV); these peaks appear at about 530.1, 532.3, 533.1, and 534.5 eV, respectively.[33] The intensity of O-I and O-II species progressively diminished with increasing temperature, whereas that of O-III increased. There was no trend found in O-IV species. A possible reorganization process of PPy during the carbonization is proposed on the basis of the XPS results in Scheme S1. To further support the proposed carbonization process, FT-IR spectroscopy was carried out. The FT-IR spectra in Figure S5 in the Supporting Information show the distinctively different absorption features before and after the carbonization, implying that restructuring of the carbon network occurred during the carbonization. Notably, peaks at 1620−1640 cm^{-1} resulting from the vibration of sp^2-carbon in graphite and a peak at 1192 cm^{-1} corresponding to C−C−C(O) stretching progressively increased with temperature, whereas a peak responsible for N═O bending at 1400 cm^{-1} and those for C−N vibration at 1381 and 1315 cm^{-1} gradually weaken (note that other detailed peak assignment is provided in Table S1).[34] This result suggests that aromatic carbon network became more robust, while nitrogen-containing surface groups were eliminated at elevated temperatures, which is in good line with our proposed scheme.

The capacitive behaviors of N-CNC_700, N-CNC_800, and N-CNC_900 were investigated using CV. Figure 5A shows the cyclic voltammograms of these three electrodes in 1 M KOH electrolyte at a scan rate of 5 mV/s. A typical rectangular response over the entire potential range was observed for all the electrodes indicating that charge storage in the N-CNC electrodes primarily occurs via the formation of an electrochemical double-layer. In addition, a couple of broad redox peaks were observed in the vicinity of 0.5 V, and these peaks were due to pseudocapacitive Faradaic reactions of the nitrogen and oxygen surface functionalities on the N-CNCs.[35−38] N-CNC_700 exhibited larger double-layer currents than N-CNC_800 and N-CNC_900 with more noticeable redox peaks suggesting that N-CNC_700 may have a better capacitance than the other samples. Figure 5B exhibits the gravimetric capacitance of three electrodes as a function of scan rate (see Figure S6 in the Supporting Information for the cyclic voltammograms of each electrode at various scan rates). As anticipated from the cyclic voltammograms, the specific capacitances of N-CNC_700 were greater than those of N-CNC_800 and N-CNC_900 for all scan rates. The specific capacitances decreased as the scan rates increased due to a limit in the diffusion rate of ions in the electrolyte. A rapid decay in the specific capacitance appeared even at slow scan rates for N-CNC_800 and N-CNC_900, but N-CNC_700 was substantially less vulnerable to capacitive loss. Based on the electrochemical results, we concluded that the capacitive behavior of N-CNC_700 was superior to those of N-CNC_800 and N-CNC_900. Note that the carbonization of PPy array was also performed at lower temperatures than 700 °C and the resulting carbon electrodes were evaluated with the hope of improving performance further. However, the electrolyte gradually turned yellowish during CV measurements, which we attributed to leaching of nonfully carbonized polymer species from the electrodes. On the basis of this observation, we concluded that PPy was not fully converted into carbon at lower temperatures than 700 °C in our experiment.

To explain why differences in capacitive performance were observed for the various N-CNCs despite their similar S_{BET} values, it is necessary to develop a comprehensive understanding of the combined effects of pore structure, specific surface area, surface functionalities, and electrical conductivity that govern the capacitive performance of N-CNCs. Several previous studies showed that not all the carbon pores contribute equally to capacitance.[39−42] For instance, Gogotsi and co-workers reported atypical enhancement in charge storage from pores less than 1 nm suggesting that pore sizes similar to the size of electrolyte ions are important for achieving high capacitance.[39] The traditional equation used to calculate the capacitance of a parallel-plate capacitor cannot be used for nanoporous carbons because the pore curvature significantly influences capacitance. To account for the effect of pore curvature, Huang and co-workers recently proposed two models that can explain the capacitance of mesoporous and microporous carbons, namely, the electric double-cylinder capacitor and the electric wire-in-cylinder capacitor models.[43] According to these models, the capacitance from mesopores (C_{meso}) and that from micropores (C_{micro}) are given by the following two equations:

$$C_{\mathrm{meso}} = \frac{\varepsilon_{\mathrm{r}}\varepsilon_0 A}{b \ln\left[\frac{b}{b-d}\right]} \tag{1}$$

$$C_{\mathrm{micro}} = \frac{\varepsilon_{\mathrm{r}}\varepsilon_0 A}{b \ln\left(\frac{b}{a_0}\right)} \tag{2}$$

where ε_r is the electrolyte dielectric constant, ε_0 is the permittivity of vacuum, A is the surface area of the electrode accessible to ions, d is the effective thickness of the electrochemical double-layer (i.e., the Debye length), b is the radius of the outer cylinder (i.e., the size of mesopores), and a_0 is the radius of the inner cylinder (i.e., the effective size of the counterions). It is worth noting that, unlike C_{meso}, C_{micro} is no longer dictated by d but is explicitly governed by a_0. This again highlights the importance of a close match between the size of the micropores and the size of the electrolyte ions in achieving higher capacitance. In addition, these theoretical predictions (which are consistent with experimental results) suggest that the mesoporous contribution (particularly for 2−5 nm pores) to capacitance gradually decreases with increasing pore size, whereas the contribution from micropores sharply rises as long as the micropores are large enough to accommodate solvated aqueous electrolyte ions.[43] Given the potential range (−1.0−0.0 V) and the electrolyte (1 M KOH) used in our CV measurement, potassium ions (K^+) are likely to serve as a primary ion species that can be adsorbed on the N-CNC surface. The size of hydrated K^+ ions is between 3.62 and 4.21 Å, while the size of hydrated OH^- ions, proposed to exist largely as an $OH^-(H_2O)_3$ complex, is estimated to be less than 5 Å.[44−46] When considering the above discussion, one could speculate that the higher capacitance of N-CNC_700 is due to a pore distribution that maximizes charge storage. While the S_{BET} values of N-CNCs were similar regardless of the carbonization temperature, the surface area of N-CNC_700 comes mainly from the contribution of micropores (S_{micro}) (Table 1). The relative portion of S_{micro} in the total surface area dramatically decreased as the carbonization temperature increased. Therefore, the higher capacitance of N-CNC_700 was attributed its broader pore distribution (down to 0.55 nm) and larger quantity of ultramicropores as compared to the other samples.

Another critical factor to consider is pseudocapacitive charge storage, which occurs through the redox reactions of nitrogen- and oxygen-containing surface functional groups. Bandosz and co-workers reported that N-5, N-6, and O-I groups are primarily responsible for the pseudocapacitive charge storage via the redox reaction of the negatively charged surface groups (N-5 and N-6) and of hydroquinone/quinone group (O—I), while N-Q and N—O groups aid electron transfer through their positive charge.[36] According to our XPS analysis (Table 2), the total amount of N and the relative amounts of N-5, N-6, and O-I groups were found to be the highest in N-CNC_700 suggesting that the pseudocapacitive contribution to the total capacitance would be greatest in N-CNC_700. This claim is partly supported by the considerably better capacitance retention of N-CNC_700 at higher scan rates because the pseudocapacitive contribution is known to dominate the double-layer capacitance at faster scan rates.[36,42] The higher N-doping level (8.5 wt %) in N-CNC_700 also plays an important role in boosting the capacitive performance by improving electrical conductivity. EIS spectra presented in Figure 5C (see Figure S7 in the Supporting Information for unmagnified spectra with an equivalent circuit employed to extract impedance components) revealed that the resistance of the electrode (R_1) and the charge-transfer resistance (R_2) are substantially smaller in N-CNC_700 than in the other two electrodes (Table 3). This is attributed to the higher incorporation of N atoms and a favorable N-6/N-Q ratio. In addition, N-CNC_700 exhibited a line with a smaller slope toward the real axis in the low frequency region as compared to N-CNC_800 and N-CNC_900 (Figure S7). This indicated that the capacitive behavior of N-CNC_700 was much closer to the ideally polarizable capacitance. This observation was in agreement with trends found in the frequency response of N-CNCs shown in Figure 5D,E. Bode plots in Figure 5D show that the capacitor response frequencies (f_0) at a phase angle of −45°, where the resistive and capacitive impedances are equal, were 0.255, 0.115, and 0.105 Hz for N-CNC_700, N-CNC_800, and N-CNC_900, respectively. The admittance plots in Figure 5E also reveal that the knee frequencies (i.e., the maximum frequency at which capacitive behavior can prevail over resistive behavior) were 825, 1.65, and 0.62 Hz for N-CNC_700, N-CNC_800, and N-CNC_900, respectively. Given that the typical knee frequencies of most commercially available supercapacitors are lower than 1 Hz,[47] this high knee frequency found in N-CNC_700 is quite remarkable. These results indicate that stored energy can reach frequencies as high as 825 Hz for N-CNC_700.

Simultaneously achieving high gravimetric (the capacitance divided by the mass of the active material) and areal capacitance (the capacitance divided by the BET surface area of the active material) is challenging. Notably, the gravimetric and areal capacitances of N-CNC_700 (Figure S8) were found to be as high as 209 F/g and 3.69 mF/cm^2 at a current density of 1 A/g. These values are substantially higher than those reported in the literature (Table S2). Capacitances obtained by both CV measurements and galvanostatic charge—discharge measurements were similar (Figure S8). Given that the galvanostatic test is regarded as the most accurate measurement of the capacitive performance,[48] the close match in capacitances measured by two techniques confirms the reliability of our results. Figure 5F displays the excellent capacitance retention of N-CNC_700 over 2000 cycles reflecting the good long-term cyclability of N-CNC_700. The performance of N-CNC_700 was further assessed in a two-electrode configuration. Figure S9 shows CV curves, galvanostatic charge—discharge profiles, and the resulting Ragone plots. While the full cell was not fully optimized for the evaluation, our preliminary results showed that the cell comprising N-CNC_700 electrodes was capable of delivering the energy density of 5.8 Wh/kg at the power density of 1000 W/kg, which is comparable to those in the literature.

Given its large surface area and high electrical conductivity, N-CNC_700 can be used as a substrate in a pseudocapacitor electrode. There have been many efforts to utilize large-surface-area, conductive substrates to overcome the common drawbacks of oxide- or hydroxide-based electrode materials (low electrical conductivity) in recent years.[49,50] As a proof of concept, we electrochemically deposited the same amount of $Ni(OH)_2$ on N-CNC_700 and a bare CFP (denoted as $Ni(OH)_2$/N-CNC and $Ni(OH)_2$/CFP) and we compared the pseudocapacitive performance of these two samples. The uniform deposition of a densely wrinkled $Ni(OH)_2$ thin layer over N-CNC_700 was confirmed by SEM and TEM analyses (Figure 6). Further evidence of $Ni(OH)_2$ formation are provided in Figure S10.

Cyclic voltammograms of $Ni(OH)_2$/N-CNC and $Ni(OH)_2$/CFP are presented in Figure 7A. A pair of redox peaks resulting from the Faradaic redox reaction ($Ni(OH)_2 + OH^- \leftrightarrow NiOOH + H_2O + e^-$) were observed, and the peak currents in the $Ni(OH)_2$/N-CNC were higher than those in the $Ni(OH)_2$/CFP. This implies better utilization of the $Ni(OH)_2$ surface when $Ni(OH)_2$ was deposited on N-CNC_700. Figure 7B exhibits the cyclic voltammograms of $Ni(OH)_2$/N-CNC as a function of scan rate. As shown, symmetric redox behavior was preserved as the scan rates increased even with an increase in specific current. This suggests that the redox reaction of $Ni(OH)_2$ had good reversibility. The gravimetric capacitances and areal capacitances of $Ni(OH)_2$/N-CNC and $Ni(OH)_2$/CFP at different scan rates are compared in parts C and D of Figure 7. Both capacitances were significantly greater in the $Ni(OH)_2$/N-CNC than in the $Ni(OH)_2$/CFP. Although a fair comparison cannot be made because of different experimental conditions (e.g., electrolyte concentrations and mass loadings of active material), the specific capacitance is comparable or even higher when compared with reports in the literature (Table S3). The mass loading of active materials has a profound effect on both specific capacitances.[48,49,51,52] A small amount of active material loaded on a substrate can provide an excellent gravimetric capacitance, but it often fails to provide a high areal capacitance. To simultaneously obtain high gravimetric and areal capacitances, it is essential to load a large amount of active material over a large-surface-area substrate to avoid dead volume (i.e., the inside of electrode not accessed by electrolyte). Therefore, a substrate can be evaluated based on its ability to achieve both high gravimetric and high areal capacitances. Given the remarkably high capacitances of N-CNC_700 (which are primarily due to the larger surface area and lower internal resistance), one can conclude that it serves as an excellent scaffold for $Ni(OH)_2$.

To further elucidate the role of N-CNC_700 in boosting the capacitances of $Ni(OH)_2$, we carried out EIS experiments. Figure 8A,B shows Nyquist plots of $Ni(OH)_2$/N-CNC and $Ni(OH)_2$/CFP, and Figure 8C displays an equivalent circuit used to extract various impedance components from the Nyquist plots. All extracted EIS parameters are summarized in Table 4. In the equivalent circuit, R_1 stands for the equivalent series resistance

(ESR), R_2 refers to the resistance involved in the adsorption/desorption of an electroactive species in parallel with the double-layer capacitance (CPE_1), R_3 is associated with charge transfer resistance in parallel with the faradaic capacitance (CPE_2) and the Warburg impedance (Z_w), and R_4 is the leakage resistance (typically ignored in the circuit because it has a very high value) in parallel with the pseudocapacitance (CPE_3).[53,54] All the resistances associated with charge transfer and internal resistance of the electrode were smaller in the $Ni(OH)_2$/N-CNC than in the $Ni(OH)_2$/CFP as were the Warburg coefficients (A_w). The smaller Warburg coefficient implies that faster ion diffusion took place when N-CNC_700 was employed as a substrate. This is attributed to the aligned carbon network on the CFP. The knee frequencies of $Ni(OH)_2$/N-CNC and $Ni(OH)_2$/CFP found in the admittance plots (Figure 8D) were 56.2 and 463.8 Hz, respectively, highlighting the superior power capability of $Ni(OH)_2$/N-CNC as compared to $Ni(OH)_2$/CFP. The complex capacitance model has served effectively as an alternative tool of EIS analysis because of its ability to describe the frequency-dependent characteristics of a supercapacitor, thus allowing the determination of an optimal frequency region for efficient power and energy delivery.[55−57] This model consists of the real (C') and imaginary (C'') capacitances that are defined by the following equations:

$$C(w) = C'(w) - iC''(w) \tag{3}$$

$$C'(w) = \frac{-Z''(w)}{w|Z(w)|^2} \quad \text{and} \quad C''(w) = \frac{Z'(w)}{w|Z(w)|^2} \tag{4}$$

Here, Z' is the real part of the impedance, Z'' is the imaginary part of the impedance, and w is the angular frequency ($2\pi f$). The real capacitance provides the frequency dependence of charge storage, while the imaginary capacitance provides information about irreversible energy loss that occurs during charge storage.[55] The normalized real and imaginary capacitances of $Ni(OH)_2$/N-CNC and $Ni(OH)_2$/CFP as a function of frequency are presented in Figure 8E,F. The characteristic frequency (f_0) (i.e., where the maximum real capacitance value is half of the maximum in Figure 8E or at the peak in the imaginary capacitance Figure 8F) is higher in the $Ni(OH)_2$/N-CNC than in the $Ni(OH)_2$/CFP. The relaxation time constants τ_0 ($= 1/f_0$) were calculated to be 10.0 and 16.1 s for the $Ni(OH)_2$/N-CNC and the $Ni(OH)_2$/CFP, respectively. Since a shorter relaxation time is linked to a faster supercapacitor response, this result indicates that energy storage and release via the redox reaction of $Ni(OH)_2$ proceeded faster when N-CNC_700 served as a substrate.

4. CONCLUSIONS

We demonstrated a facile, general method to fabricate N-doped carbon arrays on free-standing carbon substrates. In comparison to conventionally performed chemical vapor deposition methods, pyrolyzing a polypyrrole array that was electrochemically deposited on carbon fiber paper is a cost-effective, versatile approach to build N-doped carbon arrays. In addition to introducing a novel synthesis route for N-doped carbon arrays, this work showed that control over the microtextural properties and surface functionalities of the N-doped carbon array was possible simply by changing carbonization temperatures. Carbonization at low temperature (700 °C) resulted in higher content of incorporated N atoms along with the presence of pyridinic nitrogen and quinone-type oxygen. Also, unlike high-temperature carbonization (800 and 900 °C), pyrolyzing the polypyrrole array at 700 °C leads to substantially larger amounts of ultramicropores in the resulting carbon array. Our in-depth electrochemical investigation revealed that these surface characteristics played a critical role in improving the capacitive behavior of the carbon array. When utilized as a substrate for a pseudocapacitive electrode material ($Ni(OH)_2$), our N-doped carbon array allowed for high gravimetric capacitances and areal capacitances highlighting the benefit of the large surface area and high electrical conductivity of the carbon array.

■ ASSOCIATED CONTENT

Ⓢ Supporting Information

The Supporting Information is available free of charge on the ACS Publications website at DOI: 10.1021/acsami.5b05527.

Additional experimental data and analysis (PDF)

■ AUTHOR INFORMATION

Corresponding Author

*E-mail: jbang@hanyang.ac.kr.

Notes

The authors declare no competing financial interest.

■ ACKNOWLEDGMENTS

This research was supported by grants from the Basic Science Research Program through the National Research Foundation of Korea (NRF) funded by the Ministry of Science, ICT, and Future Planning (Grants NRF-2013R1A1A1008762 and 2008-0061891).

■ REFERENCES

(1) Xin, S.; Guo, Y.-G.; Wan, L.-J. Nanocarbon Networks for Advanced Rechargeable Lithium Batteries. *Acc. Chem. Res.* **2012**, *45*, 1759−1769.

(2) Guldi, D. M.; Sgobba, V. Carbon Nanostructures for Solar Energy Conversion Schemes. *Chem. Commun.* **2011**, *47*, 606−610.

(3) Dillon, A. C. Carbon Nanotubes for Photoconversion and Electrical Energy Storage. *Chem. Rev.* **2010**, *110*, 6856−6872.

(4) Shu, K.; Wang, C.; Li, S.; Zhao, C.; Yang, Y.; Liu, H.; Wallace, G. Flexible Free-Standing Graphene Paper with Interconnected Porous Structure for Energy Storage. *J. Mater. Chem. A* **2015**, *3*, 4428−4434.

(5) He, H.; Shi, L.; Fang, Y.; Li, X.; Song, Q.; Zhi, L. Mass Production of Multi-Channeled Porous Carbon Nanofibers and Their Application as Binder-Free Electrodes for High-Performance Supercapacitors. *Small* **2014**, *10*, 4671−4676.

(6) Yu, D.; Goh, K.; Wang, H.; Wei, L.; Jiang, W.; Zhang, Q.; Dai, L.; Chen, Y. Scalable Synthesis of Hierarchically Structured Carbon Nanotube-Graphene Fibres for Capacitive Energy Storage. *Nat. Nanotechnol.* **2014**, *9*, 555−562.

(7) Wang, S.; Dryfe, R. A. W. Graphene Oxide-Assisted Deposition of Carbon Nanotubes on Carbon Cloth as Advanced Binder-Free Electrodes for Flexible Supercapacitors. *J. Mater. Chem. A* **2013**, *1*, 5279−5283.

(8) Huang, Z.-D.; Zhang, B.; Oh, S.-W.; Zheng, Q.-B.; Lin, X.-Y.; Yousefi, N.; Kim, J.-K. Self-Assembled Reduced Graphene Oxide/Carbon Nanotube Thin Films as Electrodes for Supercapacitors. *J. Mater. Chem.* **2012**, *22*, 3591−3599.

(9) Dong, P.; Pint, C. L.; Hainey, M.; Mirri, F.; Zhan, Y.; Zhang, J.; Pasquali, M.; Hauge, R. H.; Verduzco, R.; Jiang, M.; Lin, H.; Lou, J. Vertically Aligned Single-Walled Carbon Nanotubes as Low-Cost and High Electrocatalytic Counter Electrode for Dye-Sensitized Solar Cells. *ACS Appl. Mater. Interfaces* **2011**, *3*, 3157−3161.

(10) Gong, K.; Du, F.; Xia, Z.; Durstock, M.; Dai, L. Nitrogen-Doped Carbon Nanotube Arrays with High Electrocatalytic Activity for Oxygen Reduction. *Science* **2009**, *323*, 760−764.

(11) Jiang, Y.; Wang, P.; Zang, X.; Yang, Y.; Kozinda, A.; Lin, L. Uniformly Embedded Metal Oxide Nanoparticles in Vertically Aligned

Carbon Nanotube Forests as Pseudocapacitor Electrodes for Enhanced Energy Storage. *Nano Lett.* **2013**, *13*, 3524−3530.

(12) Chen, Y.; Li, X.; Park, K.; Song, J.; Hong, J.; Zhou, L.; Mai, Y.-W.; Huang, H.; Goodenough, J. B. Hollow Carbon-Nanotube/Carbon-Nanofiber Hybrid Anodes for Li-Ion Batteries. *J. Am. Chem. Soc.* **2013**, *135*, 16280−16283.

(13) Hsu, Y.-K.; Chen, Y.-C.; Lin, Y.-G.; Chen, L.-C.; Chen, K.-H. High-Cell-Voltage Supercapacitor of Carbon Nanotube/Carbon Cloth Operating in Neutral Aqueous Solution. *J. Mater. Chem.* **2012**, *22*, 3383−3387.

(14) Cao, X.; Zeng, Z.; Shi, W.; Yep, P.; Yan, Q.; Zhang, H. Three-Dimensional Graphene Network Composites for Detection of Hydrogen Peroxide. *Small* **2013**, *9*, 1703−1707.

(15) Chou, S.-L.; Zhao, Y.; Wang, J.-Z.; Chen, Z.-X.; Liu, H.-K.; Dou, S.-X. Silicon/Single-Walled Carbon Nanotube Composite Paper as a Flexible Anode Material for Lithium Ion Batteries. *J. Phys. Chem. C* **2010**, *114*, 15862−15867.

(16) Chen, T.; Cai, Z.; Yang, Z.; Li, L.; Sun, X.; Huang, T.; Yu, A.; Kia, H. G.; Peng, H. Nitrogen-Doped Carbon Nanotube Composite Fiber with a Core−Sheath Structure for Novel Electrodes. *Adv. Mater.* **2011**, *23*, 4620−4625.

(17) Talapatra, S.; Kar, S.; Pal, S. K.; Vajtai, R.; Ci, L.; Victor, P.; Shaijumon, M. M.; Kaur, S.; Nalamasu, O.; Ajayan, P. M. Direct Growth of Aligned Carbon Nanotubes on Bulk Metals. *Nat. Nanotechnol.* **2006**, *1*, 112−116.

(18) Al-Mashat, L.; Debiemme-Chouvy, C.; Borensztajn, S.; Wlodarski, W. Electropolymerized Polypyrrole Nanowires for Hydrogen Gas Sensing. *J. Phys. Chem. C* **2012**, *116*, 13388−13394.

(19) Han, J. H.; Bang, J. H. A Hollow Titanium Oxynitride Nanorod Array as an Electrode Substrate Prepared by the Hot Ammonia-Induced Kirkendall Effect. *J. Mater. Chem. A* **2014**, *2*, 10568−10576.

(20) Dubal, D. P.; Lee, S. H.; Kim, J. G.; Kim, W. B.; Lokhande, C. D. Porous Polypyrrole Clusters Prepared by Electropolymerization for a High Performance Supercapacitor. *J. Mater. Chem.* **2012**, *22*, 3044−3052.

(21) Debiemme-Chouvy, C. Template-Free One-Step Electrochemical Formation of Polypyrrole Nanowire Array. *Electrochem. Commun.* **2009**, *11*, 298−301.

(22) Yang, L.; Cheng, S.; Ding, Y.; Zhu, X.; Wang, Z. L.; Liu, M. Hierarchical Network Architectures of Carbon Fiber Paper Supported Cobalt Oxide Nanonet for High-Capacity Pseudocapacitors. *Nano Lett.* **2012**, *12*, 321−325.

(23) Huang, L.; Chen, D.; Ding, Y.; Wang, Z. L.; Zeng, Z.; Liu, M. Hybrid Composite $Ni(OH)_2@NiCo_2O_4$ Grown on Carbon Fiber Paper for High-Performance Supercapacitors. *ACS Appl. Mater. Interfaces* **2013**, *5*, 11159−11162.

(24) Banerjee, A.; Bhatnagar, S.; Upadhyay, K. K.; Yadav, P.; Ogale, S. Hollow $Co_{0.85}Se$ Nanowire Array on Carbon Fiber Paper for High Rate Pseudocapacitor. *ACS Appl. Mater. Interfaces* **2014**, *6*, 18844−18852.

(25) Lee, E. J.; Bang, J. H. Mesoporous $Ni(OH)_2$ Tubes on Carbon Fiber Paper for Pseudocapacitor Electrode. *Mater. Lett.* **2013**, *105*, 28−31.

(26) Xiao, J.; Wan, L.; Yang, S.; Xiao, F.; Wang, S. Design Hierarchical Electrodes with Highly Conductive $NiCo_2S_4$ Nanotube Arrays Grown on Carbon Fiber Paper for High-Performance Pseudocapacitors. *Nano Lett.* **2014**, *14*, 831−838.

(27) Han, B.; Lee, E. J.; Kim, J. Y.; Bang, J. H. Porous Nickel Oxide Nanotube Arrays Supported on Carbon Fiber Paper: Synergistic Effect on Pseudocapacitive Behavior. *New J. Chem.* **2015**, *39*, 1996−2003.

(28) Qie, L.; Chen, W.-M.; Wang, Z.-H.; Shao, Q.-G.; Li, X.; Yuan, L.-X.; Hu, X.-L.; Zhang, W.-X.; Huang, Y.-H. Nitrogen-Doped Porous Carbon Nanofiber Webs as Anodes for Lithium Ion Batteries with a Superhigh Capacity and Rate Capability. *Adv. Mater.* **2012**, *24*, 2047−2050.

(29) Bang, J. H. Hollow Graphitic Carbon Spheres for Pt Electrocatalyst Support in Direct Methanol Fuel Cell. *Electrochim. Acta* **2011**, *56*, 8674−8679.

(30) Su, F.; Poh, C. K.; Chen, J. S.; Xu, G.; Wang, D.; Li, Q.; Lin, J.; Lou, X. W. Nitrogen-Containing Microporous Carbon Nanospheres with Improved Capacitive Properties. *Energy Environ. Sci.* **2011**, *4*, 717−724.

(31) Han, B.; Lee, E. J.; Choi, W. H.; Yoo, W. C.; Bang, J. H. Three-Dimensionally Ordered Mesoporous Carbons Activated by Hot Ammonia Treatment as High-Performance Anode Materials in Lithium-Ion Batteries. *New J. Chem.* **2015**, *39*, 6178−6185.

(32) Ding, W.; Wei, Z.; Chen, S.; Qi, X.; Yang, T.; Hu, J.; Wang, D.; Wan, L.-J.; Alvi, S. F.; Li, L. Space-Confinement-Induced Synthesis of Pyridinic- and Pyrrolic-Nitrogen-Doped Graphene for the Catalysis of Oxygen Reduction. *Angew. Chem., Int. Ed.* **2013**, *52*, 11755−11759.

(33) Zhou, J.-H.; Sui, Z.-J.; Zhu, J.; Li, P.; Chen, D.; Dai, Y.-C.; Yuan, W.-K. Characterization of Surface Oxygen Complexes on Carbon Nanofibers by TPD, XPS and FT-IR. *Carbon* **2007**, *45*, 785−796.

(34) Zhang, B.; Yu, Y.; Xu, Z.-L.; Abouali, S.; Akbari, M.; He, Y.-B.; Kang, F.; Kim, J.-K. Correlation between Atomic Structure and Electrochemical Performance of Anodes Made from Electrospun Carbon Nanofiber Films. *Adv. Energy Mater.* **2014**, *4*, 1301448.

(35) Zhao, L.; Fan, L.-Z.; Zhou, M.-Q.; Guan, H.; Qiao, S.; Antonietti, M.; Titirici, M.-M. Nitrogen-Containing Hydrothermal Carbons with Superior Performance in Supercapacitors. *Adv. Mater.* **2010**, *22*, 5202−5206.

(36) Hulicova-Jurcakova, D.; Seredych, M.; Lu, G. Q.; Bandosz, T. J. Combined Effect of Nitrogen- and Oxygen-Containing Functional Groups of Microporous Activated Carbon on Its Electrochemical Performance in Supercapacitors. *Adv. Funct. Mater.* **2009**, *19*, 438−447.

(37) Fang, Y.; Luo, B.; Jia, Y.; Li, X.; Wang, B.; Song, Q.; Kang, F.; Zhi, L. Renewing Functionalized Graphene as Electrodes for High-Performance Supercapacitors. *Adv. Mater.* **2012**, *24*, 6348−6355.

(38) Chen, L.-F.; Zhang, X.-D.; Liang, H.-W.; Kong, M.; Guan, Q.-F.; Chen, P.; Wu, Z.-Y.; Yu, S.-H. Synthesis of Nitrogen-Doped Porous Carbon Nanofibers as an Efficient Electrode Material for Supercapacitors. *ACS Nano* **2012**, *6*, 7092−7102.

(39) Chmiola, J.; Yushin, G.; Gogotsi, Y.; Portet, C.; Simon, P.; Taberna, P. L. Anomalous Increase in Carbon Capacitance at Pore Sizes Less Than 1 Nanometer. *Science* **2006**, *313*, 1760−1763.

(40) Largeot, C.; Portet, C.; Chmiola, J.; Taberna, P.-L.; Gogotsi, Y.; Simon, P. Relation between the Ion Size and Pore Size for an Electric Double-Layer Capacitor. *J. Am. Chem. Soc.* **2008**, *130*, 2730−2731.

(41) Chmiola, J.; Largeot, C.; Taberna, P.-L.; Simon, P.; Gogotsi, Y. Desolvation of Ions in Subnanometer Pores and Its Effect on Capacitance and Double-Layer Theory. *Angew. Chem., Int. Ed.* **2008**, *47*, 3392−3395.

(42) Raymundo-Piñero, E.; Kierzek, K.; Machnikowski, J.; Béguin, F. Relationship between the Nanoporous Texture of Activated Carbons and Their Capacitance Properties in Different Electrolytes. *Carbon* **2006**, *44*, 2498−2507.

(43) Huang, J.; Sumpter, B. G.; Meunier, V. A Universal Model for Nanoporous Carbon Supercapacitors Applicable to Diverse Pore Regimes, Carbon Materials, and Electrolytes. *Chem. - Eur. J.* **2008**, *14*, 6614−6626.

(44) Eliad, L.; Salitra, G.; Soffer, A.; Aurbach, D. Ion Sieving Effects in the Electrical Double Layer of Porous Carbon Electrodes: Estimating Effective Ion Size in Electrolytic Solutions. *J. Phys. Chem. B* **2001**, *105*, 6880−6887.

(45) Tuckerman, M. E.; Marx, D.; Parrinello, M. The Nature and Transport Mechanism of Hydrated Hydroxide Ions in Aqueous Solution. *Nature* **2002**, *417*, 925−929.

(46) Mähler, J.; Persson, I. A Study of the Hydration of the Alkali Metal Ions in Aqueous Solution. *Inorg. Chem.* **2012**, *51*, 425−438.

(47) Chunsheng, D.; Ning, P. High Power Density Supercapacitor Electrodes of Carbon Nanotube Films by Electrophoretic Deposition. *Nanotechnology* **2006**, *17*, 5314−5318.

(48) Zhang, S.; Pan, N. Supercapacitors Performance Evaluation. *Adv. Energy Mater.* **2015**, *5*, 1401401.

(49) Xia, X.; Tu, J.; Zhang, Y.; Wang, X.; Gu, C.; Zhao, X.-b.; Fan, H. J. High-Quality Metal Oxide Core/Shell Nanowire Arrays on Conductive Substrates for Electrochemical Energy Storage. *ACS Nano* **2012**, *6*, 5531−5538.

(50) Zhang, G.; Lou, X. W. General Solution Growth of Mesoporous $NiCo_2O_4$ Nanosheets on Various Conductive Substrates as High-Performance Electrodes for Supercapacitors. *Adv. Mater.* **2013**, *25*, 976−979.

(51) Liu, J.; Jiang, J.; Cheng, C.; Li, H.; Zhang, J.; Gong, H.; Fan, H. J. Co_3O_4 Nanowire@MnO_2 Ultrathin Nanosheet Core/Shell Arrays: A New Class of High-Performance Pseudocapacitive Materials. *Adv. Mater.* **2011**, *23*, 2076−2081.

(52) Kwak, J. H.; Lee, Y.-W.; Bang, J. H. Supercapacitor Electrode with an Ultrahigh Co_3O_4 Loading for a High Areal Capacitance. *Mater. Lett.* **2013**, *110*, 237−240.

(53) Li, M.; Xu, S.; Liu, T.; Wang, F.; Yang, P.; Wang, L.; Chu, P. K. Electrochemically-Deposited Nanostructured $Co(OH)_2$ Flakes on Three-Dimensional Ordered Nickel/Silicon Microchannel Plates for Miniature Supercapacitors. *J. Mater. Chem. A* **2013**, *1*, 532−540.

(54) Wang, W.; Guo, S.; Lee, I.; Ahmed, K.; Zhong, J.; Favors, Z.; Zaera, F.; Ozkan, M.; Ozkan, C. S. Hydrous Ruthenium Oxide Nanoparticles Anchored to Graphene and Carbon Nanotube Hybrid Foam for Supercapacitors. *Sci. Rep.* **2014**, *4*, 4452.

(55) Taberna, P. L.; Portet, C.; Simon, P. Electrode Surface Treatment and Electrochemical Impedance Spectroscopy Study on Carbon/Carbon Supercapacitors. *Appl. Phys. A: Mater. Sci. Process.* **2006**, *82*, 639−646.

(56) Choi, B. G.; Hong, J.; Hong, W. H.; Hammond, P. T.; Park, H. Facilitated Ion Transport in All-Solid-State Flexible Supercapacitors. *ACS Nano* **2011**, *5*, 7205−7213.

(57) Yao, Y.; Ma, C.; Wang, J.; Qiao, W.; Ling, L.; Long, D. Rational Design of High-Surface-Area Carbon Nanotube/Microporous Carbon Core−Shell Nanocomposites for Supercapacitor Electrodes. *ACS Appl. Mater. Interfaces* **2015**, *7*, 4817−4825.